Evolution of Boride Morphologies in TiAl-B Alloys

M.E. HYMAN, C. McCULLOUGH, C.G. LEVI, and R. MEHRABIAN

The solidification of γ-TiAl alloys with relatively low (<2 at. pct) additions of boron is discussed. Binary Ti-Al alloys containing 49 to 52 at. pct Al form primary α-(Ti) dendrites from the melt, which are subsequently surrounded by γ segregate as the system goes through the peritectic reaction $L + \alpha \rightarrow \gamma$. Alloys between 45 and 49 at. pct Al go through a double peritectic cascade, forming primary β-(Ti) surrounded by α-(Ti) and eventually by γ in the interdendritic spaces. Boron additions to these binary alloys do not change the basic solidification sequence of the matrix but introduce the refractory compound TiB_2 in a variety of morphologies. The boride develops as highly convoluted flakes in the leaner alloys, but needles, plates, and equiaxed particles gradually appear as the B content increases above ~1 at. pct. Increasing the solidification rate initially promotes the formation of flakes over plates/needles and ultimately gives way to very fine equiaxed TiB_2 particles in the interdendritic spaces of the metallic matrix. Furthermore, the primary phase selection in the 49 to 52 at. pct Al range changes from α-(Ti) to β-(Ti) at supercoolings of the order of 200 K. The different boride morphologies are fully characterized, and their evolution is rationalized in terms of differences in their nucleation and growth behavior and their relationship to the solidification of the intermetallic matrix.

I. INTRODUCTION

DEVELOPMENT of engineering alloys based upon γ-TiAl requires increasing toughness and creep strength while maintaining the attractive modulus and oxidation resistance of the intermetallic compound. Promising toughness values have been produced by dispersions of Ti-Nb alloy ductile phases in γ-TiAl,[1] but this benefit seems to be accompanied by a reduction in high-temperature creep strength.[2] Most current efforts to enhance the creep properties of γ alloys involve refractory second phases that would constrain the plastic flow of the matrix during high-temperature service. Micromechanics considerations indicate that these reinforcements must have morphologies with high aspect ratios (*i.e.*, fibers, rods, plates) and a long dimension appreciably larger than the dislocation cell size (*i.e.*, a few micrometers).[3,4]

Reinforcing phases may be incorporated in the aluminide matrix by compositing techniques or may be grown *in situ* by suitable design of the alloy chemistry and processing route. In one novel approach, TiB_2 and other refractory compounds are grown by reaction of the constituent elements in a molten metal solvent, typically Al, yielding a "master" composite which is subsequently alloyed with the proper amounts of Ti, Al, *etc.*, to reach the desired intermetallic matrix composition.[5] A peculiar feature of this approach is that the strengthening phase remains largely undissolved during the final alloying stage. This allows for lower processing temperatures but may limit the composite stability if the compound that grows in the original solvent metal (Al) is not a phase that can achieve equilibrium with the final matrix. Alternatively, reinforcements may be grown as primary phases from a melt with the proper chemistry. For example, Ti_2AlC plates with aspect ratios of ~20 and volume fractions up to ~0.12 have been produced in γ alloys with ~3 pct C.[6]* Preliminary results indicate that both routes result in materials with improved creep resistance,[7–10] but the strengthening contribution of the reinforcements is obscured by concomitant changes in the matrix grain size and solute content.

*All compositions are in atomic percent unless specified otherwise.

A fundamental understanding of the mechanisms that control the size and shape of reinforcements grown from the melt is clearly desirable. Previous work by the authors revealed that TiB_2 exhibits various morphologies when growing from Ti-Al melts of approximately equiatomic composition with additions of 0.9 and 5.4 pct B.[11] The alloys higher in boron form primary TiB_2 which grows as blocky (approximately equiaxed) faceted particles 10 to 20 μm across, in agreement with the anticipated growth pattern for this boride which has the hexagonal C32 structure. The leaner alloys only form small amounts of nonequiaxed (presumably secondary) boride particles, which may evolve as plates, needles, and/or flakes. These elongated morphologies were tentatively ascribed to the constraint imposed by the matrix on the (secondary) borides as they grow concurrently from the melt.[11]

The present investigation was undertaken to elucidate the origin of the multiple TiB_2 morphologies in γ-TiAl + B alloys and to study their dependence on important solidification parameters like bulk supercooling and cooling rate. Of particular interest were the potential for controlling the boride phase morphology, distribution and size scale by solidification processing, and the concomitant effects on the evolution of the matrix microstructure. The research focused on alloys containing 45

M.E. HYMAN, formerly Research Assistant, University of California–Santa Barbara (UCSB), is Environmental Engineer with Engineering Management Concepts, Camarillo, CA 93010. C. McCULLOUGH, Assistant Research Engineer, Materials Department, and C.G. LEVI, Associate Professor of Materials and Mechanical and Environmental Engineering, are with UCSB, Santa Barbara, CA 93106. R. MEHRABIAN, formerly Professor of Materials and Dean of the College of Engineering at UCSB, is President, Carnegie Mellon University, Pittsburgh, PA 15213-3890.

Manuscript submitted July 16, 1990.

to 52 pct Al and up to ~1.6 pct B (Table I), largely because higher boron contents form significant amounts of primary TiB_2 and exhibit little or no potential for supercooling.

II. EXPERIMENTAL

The selected experimental approach involved electromagnetic levitation and melting followed by gas cooling and/or splat quenching with a double-anvil device. These techniques permit the monitoring of part or all of the thermal history and the establishment of more quantitative relationships with microstructural observations. They have been applied quite successfully to studies of various binary and ternary γ-TiAl alloys.[12]

The alloys were prepared by arc melting in a gettered-argon atmosphere (<0.1 ppb O_2) using high-purity Ti buttons (<200 ppm O), Al pellets (99.99 pct Al), and nitrogen-free B powder (99.7 pct B, 60 mesh).* Extensive precautions were taken to avoid N contamination, which was previously found to produce spurious ternary nitrides that complicate the interpretation of the microstructures.[11] The materials were melted following the procedure established in a previous publication,[11] wherein B is first dissolved in Ti to form homogeneous Ti-B master alloy and Al is subsequently added to achieve the desired matrix composition. Aluminum losses can be minimized in this manner, because the Ti-B master alloy melts at temperatures lower than those necessary to dissolve elemental B in molten TiAl. Some buttons were cut into pieces ~400 mg in weight, which were then remelted into spheres ~4 mm in diameter, suitable for the levitation experiments.

*Titanium buttons were supplied by Timet, Henderson, NV; Al pellets and B powder by Alfa/Johnson-Matthey, Ward Hill, MA.

Table I. Alloy Compositions Investigated*

Alloy	Pct Al	Pct B
5103	51.1	0.33
4907**	49.1	0.72
5107	50.9	0.71
5208	51.7	0.82
5009	50.3	0.85
4510	45.2	0.98
4910	49.4	1.00
5010	50.3	0.99
5210	51.9	0.95
4712	46.9	1.15
4912	48.6	1.24
5212†	51.5	1.15
5013	50.4	1.33
4915	49.2	1.54
5016	50.4	1.60

*Balance Ti. All compositions in atomic percent. Aluminum by atomic absorption spectroscopy; boron by DC plasma emission spectroscopy. Aluminum compositions verified by energy-dispersive spectroscopy in the scanning electron microscope.

**Main alloy used for studying dependence of microstructure on supercooling.

†Main alloy used for studying dependence of microstructure on cooling rate.

The two configurations of the experimental apparatus used in this investigation are schematically depicted in Figure 1. In general, the sample was suspended in a flow of Ar gas within a PYREX* tubular chamber by means of a levitation coil driven by a 20 kW, 450 kHz radio frequency (RF) power supply. The chamber was built with an expanded middle section to prevent contact between the walls and the sample as the latter undergoes vibrational, rotational, and oscillatory motions due to dynamic interactions with the RF field during melting.[13] Once liquid, the sample was superheated and held for about 30 to 90 seconds to permit dissolution of the refractory phases and homogenization of the melt. Temperature control in this period is critical to avoid evaporation of Al and is effected by manipulating the power level and gas flow. The liquid droplet could then be quenched by switching to a rapid flow of He gas (Figure 1(a)) or dropped between two electromagnetically driven Cu-Be anvils (Figure 1(b)). The anvils were polished to a 50 nm Al_2O_3 finish and triggered by a photodetector which is activated by the sample radiation. The splats produced in this setup ranged from 50 to 150 μm thick.

*PYREX is a trademark of Corning Glass Works, Corning, NY.

The thermal history of the samples (through solidification or until the moment of splatting) was monitored by a fast-response (40 Hz) Ircon-Maxline two-color pyrometer and recorded to disk on a microcomputer. The pyrometer was calibrated for the temperature range of interest using an emissivity correction factor of 1.07, determined from the melting point of a pure Ti standard.*

*It is assumed that the emissivity of the alloys is similar to that of the clean, unoxidized pure metal and does not depend on alloy composition.

Given a minimum target area of 2 mm and an instrument

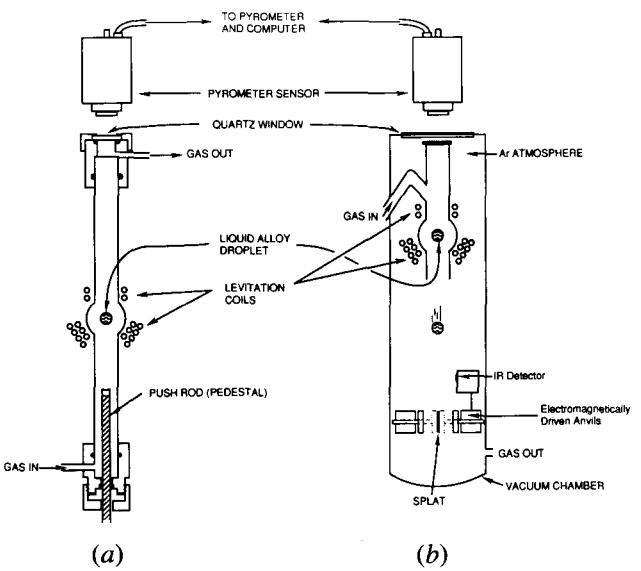

Fig. 1—Schematic diagram of electromagnetic levitation/melting apparatus: (*a*) configuration used for supercooling and gas-cooling experiments and (*b*) configuration used for splat-quenching experiments.

repeatability of 0.1 pct of full scale (2086 K), the accuracy of the temperature measurements should be within ±2 K.

Figure 2 depicts a schematic thermal history for a sample that was completely solidified by He gas cooling. The thermal arrest upon heating represents the melting process, which is followed by rapid superheating and a holding period at a constant temperature above the liquidus. The liquid is then rapidly cooled until nucleation of the primary phase occurs, leading to recalescence. The supercoolings reported here were determined from the extent of the recalescence excursion and thus are slightly underestimated.[12] Thermal arrests after recalescence are associated with the nucleation of secondary phases during solidification. Samples with no distinguishable recalescence are assumed to nucleate without appreciable supercooling, and their microstructures should reflect primarily the effects of the cooling rate, which can be determined from the slope of the thermal history curve.

The solidified specimens were sectioned, polished, and etched for characterization by optical and scanning electron microscopy (SEM) in secondary electron mode. The matrix phases and larger boride particles were conveniently revealed for optical examination using the electrolytic staining technique described in a previous publication.[11] Additional studies of the boride morphologies were made on samples electrolytically deep-etched using a solution of 7 vol pct HCl in methanol and a voltage of 20 VDC for 30 to 45 seconds. Transmission electron microscopy (TEM) was performed on specimens electropolished in a perchloric acid/butanol/methanol solution following the procedure described in earlier publications.[14,15] Since the thicker boride particles were not thinned by electropolishing, their TEM analysis required dimpling and ion milling at 5 kV, 1 mA, with Ar ions. Finally, two-stage TEM extraction replicas from the deep-etched samples were used to facilitate the examination of the thinner borides and the correlation of crystallographic information to the external features of the different morphologies.

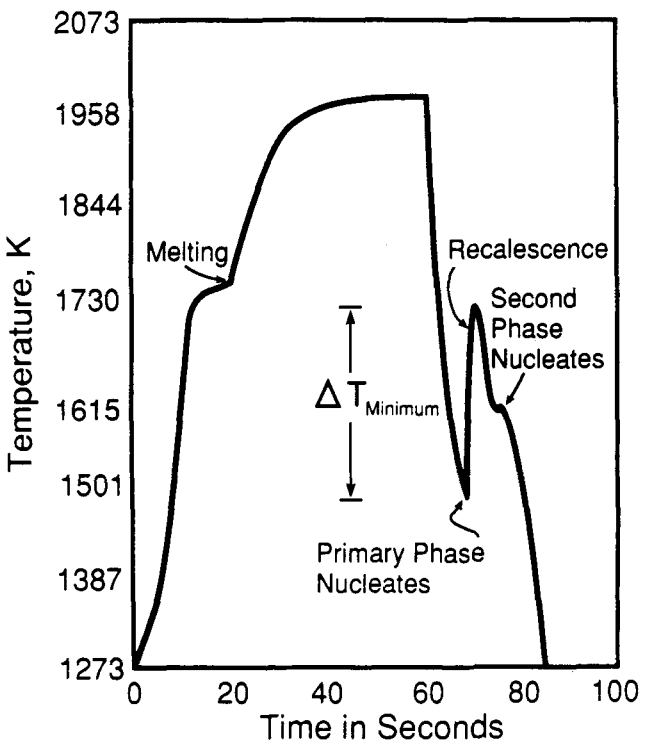

Fig. 2—Typical thermal history curve of a supercooled droplet showing two nucleation events. The extent of supercooling is determined from the initial recalescence excursion.

III. RESULTS AND DISCUSSION

The characteristics of the different boride morphologies observed in this investigation are summarized in Table II. For the relatively dilute alloys studied, a large fraction of the borides grow concurrently with the metallic matrix and, hence, are significantly influenced by the presence of the latter. Thus, we shall focus first on the broader aspects of the microstructure, which pertain to the evolution of the matrix microconstituents under conventional and rapid solidification conditions, noting where appropriate the morphological characteristics of the boride phases. Subsequently, we will discuss the crystallographic aspects of the different boride morphologies and attempt to shed some light on their evolution.

A. *Conventional Solidification*

The conventional solidification path for γ alloys containing 49 to 52 pct Al and ~1 pct B closely parallels that of binary Ti-Al alloys of similar composition. The recently revised Ti-Al phase diagram in Figure 3[14,16] suggests that the matrix in these alloys should solidify as α-(Ti) dendrites surrounded by γ-TiAl segregate in the interdendritic spaces. This is confirmed by optical examination of the as-cast ternary buttons in Figures 4(a) and (b), where the hexagonal symmetry of the α-(Ti) dendrites is clearly evident. Also note in this figure that the proportion of γ segregate increases quite rapidly with Al content. Alloys below 49 pct Al (*e.g.*, 4510 and 4712 in Table I) show evidence of having formed cubic β-(Ti) at the start of solidification, as expected from the binary phase diagram.

The γ segregate is stable and can be retained through the post-solidification cooling. However, the primary α phase undergoes a series of solid-state transformations which eventually yield the characteristic "lath" microconstituent manifested as striations within the dendrites in Figure 4. The latter has been shown to consist of alternating lamellae of α_2 and two twin-related variants of γ with the close-packed planes and directions in the two phases parallel to each other.[14]

The boride phases in the conventionally solidified alloys appear in four distinct morphologies: convoluted flakes, plates, needles, and blocky particles. These are illustrated for alloys of ~50 pct Al and increasing B concentration in Figure 5.* The leanest alloy in Table I (5103), with 0.33B, contains only flakes which are clearly

*The plate morphology is not easily distinguishable from the needles in polished sections, but it will be evident in the micrographs of deeply etched specimens presented later.

Table II. Summary of TiB_2 Morphologies Observed

Morphology	Typical Short Dimension	Aspect Ratio	Dominant Facets	Origin
Blocky	10 to 20 μm	~ 1	$\{10\bar{1}0\}$ (0001)	Primary borides; nucleate and grow unconstrained in melts with B contents substantially above monovariant line.
Plates	≤2 μm	10 to 20	$\{10\bar{1}0\}$	Believed to nucleate as primary borides near monovariant line but are soon trapped and constrained by evolving matrix.
Needles	≤2 μm	10 to 20	$\{10\bar{1}0\}$	Develop from plates due to morphological instability induced by diffusional constraints.
Flakes	≤0.5 μm	20 to 100	$\{1\bar{2}10\}$	True secondary borides. Nucleate after primary metallic phase, perhaps in contact with it, and grow coupled with matrix. Convoluted morphology typical of irregular eutectic growth.
Fine particles	≤250 nm	~ 1	$\{10\bar{1}0\}$ (0001)	Secondary borides in rapidly solidified alloys with B contents below ~1 pct. Evolve from "massive" nucleation in highly supersaturated liquid within interdendritic spaces of primary metallic phase.
Fine platelets	~ 10 nm	<10	N/D*	Solid-state precipitates evolved during cooling from a supersaturated matrix. Detectable only in specimens supercooled ≥200 K, suggesting solute trapping during rapid solidification.

*N/D = not determined.

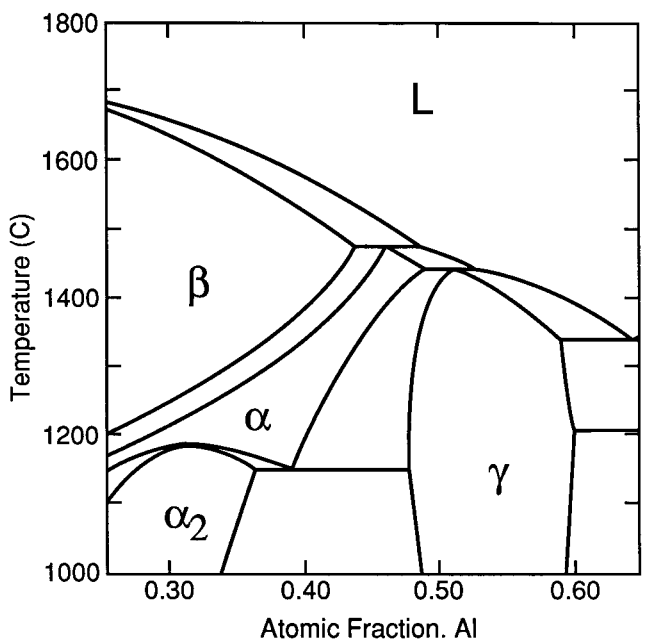

Fig. 3—Binary Ti-Al diagram incorporating recent revision of the phase equilibria in the vicinity of the γ field.[14,16]

associated with the interdendritic γ segregate, as noted in Figure 5(a). As the B content increases to ~0.7 pct (4907, 5107), the flakes appear mixed with both dendrites and segregate, as illustrated in Figure 5(b). Plates and needles are first observed above ~0.8 pct B (5208, 5009) but always in combination with the flakes. In general, all of these elongated particles have thicknesses below ~2 μm, as noted in Table II. Blocky particles, equiaxed and somewhat larger in size, evolve in addition to the other morphologies for alloys above ~1 pct B (*e.g.*, Figures 5(c) and (d)). In richer alloys, these particles can grow to be 10 to 20 μm across and are not particularly associated with either dendrites or segregate.[11] It is reasonably clear from these observations that the convoluted flakes are secondary borides which grow concurrently with the γ and/or α phases during solidification, whereas the blocky particles are primary TiB_2 forming prior to the nucleation of any metallic phase. The origin of the plates and needles is not immediately obvious and will be discussed in a later section.

The microstructural evidence suggests that the ternary liquidi surfaces in the region of interest are related, as depicted schematically in Figure 6. The TiB_2 liquidus originating at the Ti-B binary intersects the β, α, and γ

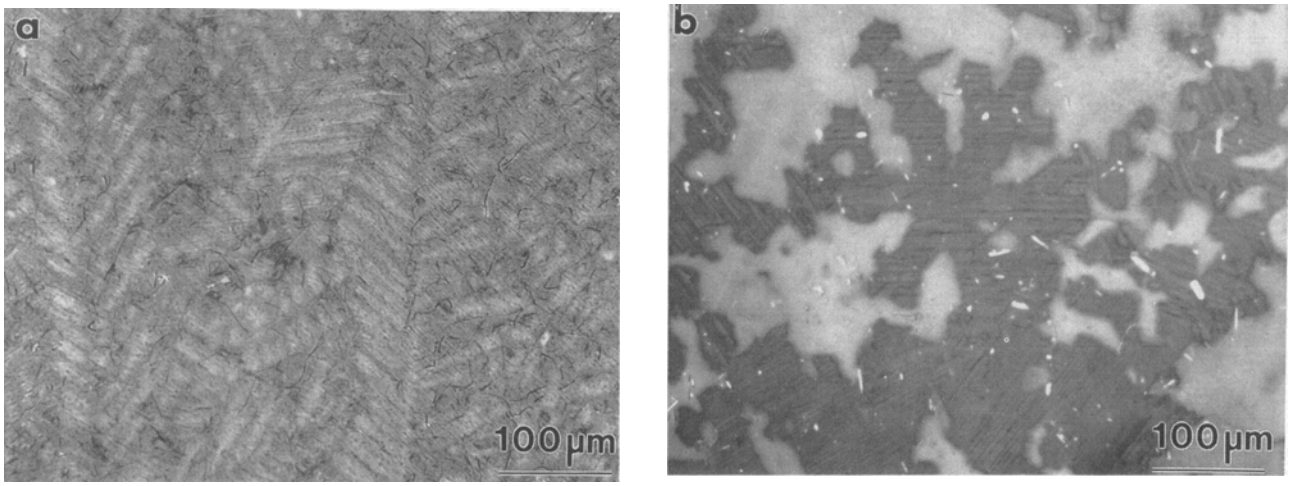

Fig. 4—Optical micrographs of as-cast buttons electrolitically etched: (*a*) alloy 4910 (49.4 pct Al-1 pct B) showing columnar α-(Ti) dendrites near the chill face and (*b*) alloy 5212 (51.5 pct Al-1.15 pct B) showing increased amounts of γ segregate surrounding an equiaxed α-(Ti) dendrite and some primary TiB_2 particles.

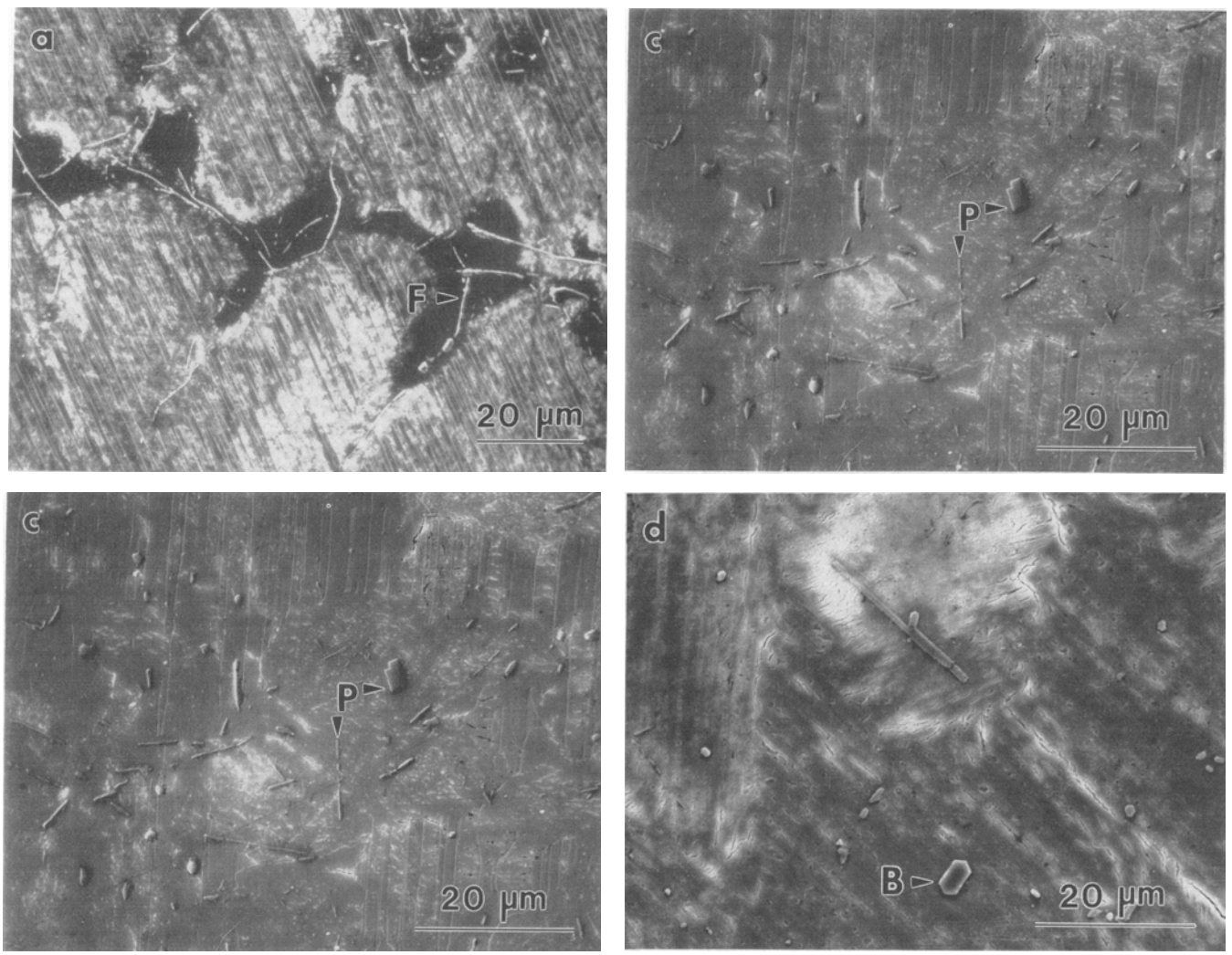

Fig. 5—Evolution of boride morphologies with increasing boron content for nearly equiatomic Ti-Al buttons: (*a*) alloy 5103 (0.33 pct B), (*b*) alloy 5107 (0.71 pct B), (*c*) alloy 5010 (0.99 pct B), and (*d*) alloy 5013 (1.33 pct B). Arrows denote (F)lakes, (P)lates/needles, and (B)locky primaries.

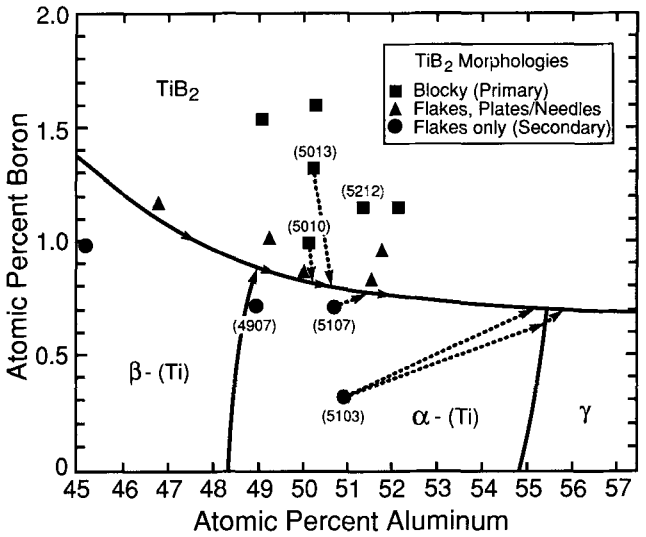

Fig. 6—Suggested liquidus projection for the ternary Ti-Al-B system in the vicinity of the equiatomic TiAl composition. The lower boundary of the TiB_2 field is a twofold saturation line; the boundaries between β/α and α/γ are extensions of the binary peritectics in Fig. 3. Dashed lines denote schematic solidification paths for the alloys in Fig. 5.

fields emerging from the Ti-Al binary near the 1 pct B isoconcentrate and forms a descending monovariant line of the type $L \rightarrow M + TiB_2$, where the metallic phases (M) evolve in the same sequence as in the double peritectic cascade of the binary diagram: $M = \beta \rightarrow \alpha \rightarrow \gamma$.

The solidification paths of the alloys in Figure 5 may now be elucidated with the aid of the diagram in Figure 6. Alloys 5103 and 5107 form primary α with lower Al content than the melt (~46 pct based on the binary Ti-Al) and (presumably) negligible B in solution. Thus, the composition of the liquid should move away from the Ti-Al binary and toward the monovariant line. Since there is no significant amount of boride within the dendrites of the leaner alloy (5103), its solidification path must intersect the monovariant line very close to the ternary reaction $L + \alpha \rightarrow \gamma + TiB_2$, as illustrated in Figure 6. The alloy might then form, first, a small amount of TiB_2 and, shortly thereafter, γ or *vice versa*. On the other hand, alloy 5107 contains enough B that it can only form a small amount of primary α before reaching the twofold saturation line, wherein TiB_2 flakes would first grow concurrently with α and subsequently with γ in the interdendritic spaces. Conversely, alloys 5010 and 5013 would form primary TiB_2 and move toward the Ti-Al binary until the liquid composition reaches the monovariant line, at which point α and secondary TiB_2 would evolve concurrently from the melt (Figure 6).

B. *Effect of Supercooling*

Boron additions were found to rapidly curtail the undercoolability of molten γ-base alloys. Prior levitation-melting studies revealed that nucleation could be readily suppressed in the binary alloys, with the achievable supercooling increasing from 262 K for Ti-45 pct Al to 384 K for Ti-55 pct Al.[12] However, no appreciable supercooling could be produced in any of the alloys above 1 pct B (*e.g.*, 4915 or 5212), presumably because primary TiB_2 is readily formed and triggers the nucleation of the metallic phase. Lower B alloys did supercool quite significantly; for example, alloy 4907 (0.72 pct B) achieved a maximum ΔT of 278 K, which is comparable to the 286 K produced in the binary Ti-50 pct Al alloy,[12] while three other alloys ranging from 0.82 to 1.0 pct B (4910, 5009, and 5208) achieved supercoolings of the order of 200 K.

The effects of supercooling on the solidification microstructure are similar for all of the alloys noted above and are illustrated for the leaner B composition (4907) in Figure 7. The conventional solidification path for this alloy is essentially the same as that for alloy 5107 above, except for a much reduced proportion of γ segregate consistent with the lower Al content of 4907. At $\Delta T \sim$ 100 K, the microstructure is not much different from the arc button material, except for a slight reduction in the amount of segregate. The primary phase selected from the melt is still α-(Ti), as suggested by the hexagonal dendrite in Figure 7(a), and the boride develops the flake morphology (Figure 7(c)). As the supercooling increases above ~150 K, both the matrix and the boride phase experience substantial refinement, as shown in Figures 7(b) and (d). Dendrites are no longer evident in the microstructure, and the borides appear as very fine ($\lesssim$250 nm) equiaxed crystals which vaguely seem to delineate dendrite or cell boundaries (compare with Figure 9(e)).

Transmission electron microscopy analyses of alloy 4907 samples supercooled to 218 and 278 K reveal very similar microstructures. The matrix consists of well-developed packets of the ($\alpha_2 + \gamma$) lath microconstituent, as shown for the higher supercooling in Figure 8(a). The prior α grain (or lath packet) size ranges from 5 to 20 μm in this sample, compared with the 100 to 200 μm grain size associated with the dendritic microstructures. Upon closer examination (Figure 8(b)), the laths were seen to contain very fine platelike borides with the external crystallographic features of TiB_2 and dimensions of 20 to 50 nm wide by ~10 nm thick. These platelets are significantly smaller than the fine equiaxed boride particles in Figure 7(d), as evident from the higher magnification view of the latter in Figure 17, and hence are believed to be a product of solid-state precipitation rather than solidification. The population of these ultrafine boride platelets is only significant at $\Delta T > 200$ K and increases with the initial supercooling, suggesting a progressive extension of B solubility produced by the concomitantly higher interface velocities.

Selected area diffraction (SAD) of neighboring lath packets revealed that their habit planes frequently form 120 deg angles with each other. For example, the $\{111\}_\gamma$ habit planes of the three lath packets in Figure 8(c) are all viewed end-on down the $[1\bar{1}0]_\gamma$ zone axis, as shown by the SAD pattern of one of the packets in Figure 8(d). It has been shown elsewhere that the $\{111\}_\gamma$ planes of the γ variants in the lath are parallel to the basal plane of the residual α_2 and hence to the basal planes of the parent α.[15,17] Thus, the three packets depicted in this figure originated from three neighboring α grains which had their (0001) planes mutually oriented at 120 deg angles.

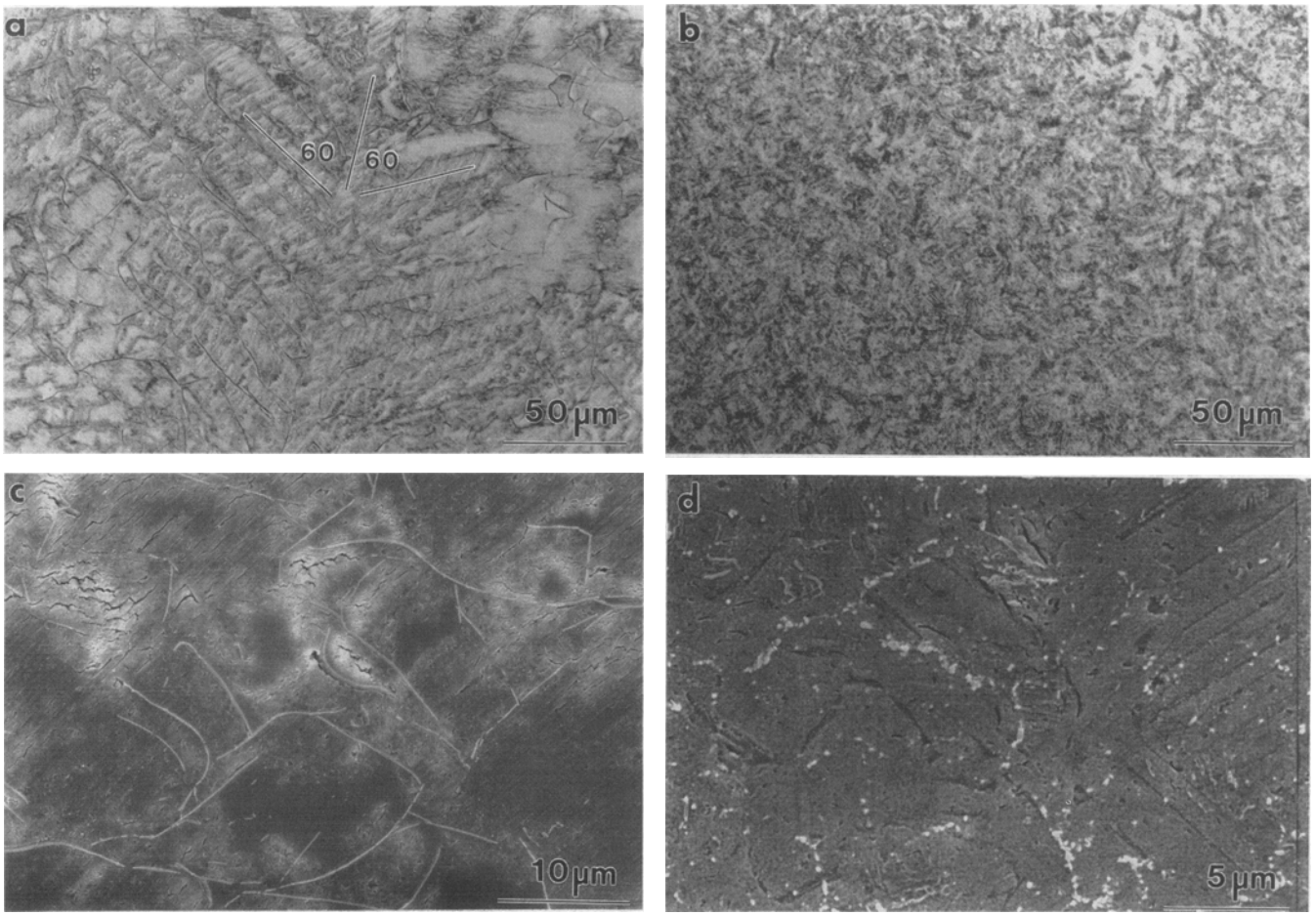

Fig. 7—Microstructures of supercooled alloy 4907 (0.72 pct B): (*a*) and (*c*) show primary α-Ti and flake TiB_2 after $\Delta T = 100$ K; (*b*) and (*d*) show fine-grained microstructure with small equiaxed borides after $\Delta T = 218$ K.

This is precisely what would be expected if the α grains evolved from a solid-state transformation of a single grain of β phase following the Burgers orientation relationship:[18]

$$(0001)_\alpha \parallel \{110\}_\beta; \qquad \langle 1\bar{2}10\rangle_\alpha \parallel \langle 111\rangle_\beta \qquad [1]$$

The γ laths would then be related back to the original β phase in the following manner:*

*Note that this is not an actual orientation relationship but describes the effective crystallographic relation between two phases that never existed together.

$$\{110\}_\beta \rightarrow \{111\}_\gamma; \qquad \langle 111\rangle_\beta \rightarrow \langle 1\bar{1}0\rangle_\gamma \qquad [2]$$

Thus, the evidence suggests that the fine microstructure of the highly supercooled samples results from the solid-state transformation of a metastable primary β phase selected from the liquid. This is consistent with recent work on the phase selection hierarchies in the binary Ti-Al system, where β was found to be the kinetically preferred phase at high supercoolings even in the composition range where α and/or γ have a larger thermodynamic driving force for soldification.[12]

One could also argue that the apparent increase in B supersaturation observed above $\Delta T \sim 200$ K may be associated with the change in the primary phase selection from α to β. Boron is normally considered an interstitial solute, but its relatively large atomic size drastically limits the solubility in both structures, and more so in the β phase, which has smaller interstices. There is evidence, however, that large supersaturations of B may be produced in β-(Ti) by rapid solidification,[19] presumably because a sizable fraction of the B is trapped as a substitutional element. The excess B would readily precipitate in the post-recalescence period, as the cooling rates characteristic of the gas quenching process are relatively modest.

C. *Effect of Cooling Rate*

While the different boride morphologies (plates/needles/flakes) were present throughout the microstructures of all buttons above ~0.8B, it was clearly evident that the flakes tend to be more numerous near the chill surfaces, suggesting an influence of the cooling rate on the growth pattern of the boride phases. Hence, a series of experiments were undertaken to assess the effects of varying quenching conditions on the microstructure. To isolate these effects from those arising from bulk supercooling, the analysis was limited to samples showing negligible recalescence excursions in the thermal history curve. (This can only be ascertained in the

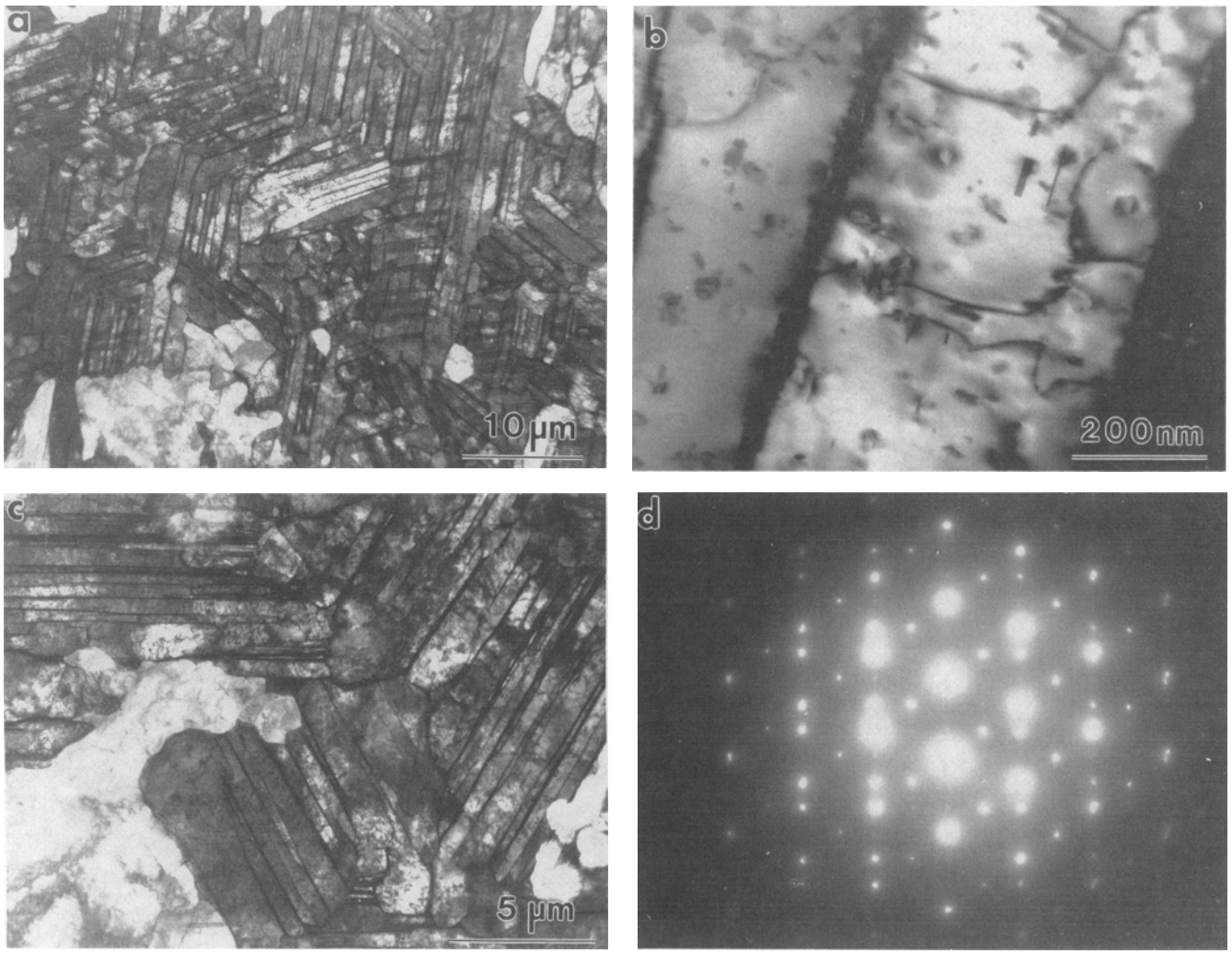

Fig. 8—TEM micrographs of alloy 4907 (0.72 pct B) supercooled to 278 K, revealing (*a*) packets of $\alpha_2 + \gamma$ lath with small amounts of γ segregate, (*b*) ultrafine boride precipitates within γ laths, (*c*) three lath variants with their habit planes oriented 120 deg from each other, and (*d*) SAD pattern from a single lath packet showing two twin related $[1\bar{1}0]\gamma$ zones and a very faint single $[1\bar{2}10]\alpha_2$ zone.

gas cooling experiments but not in the splat quenching, where the thermal history cannot be followed after the sample is dropped between the anvils.) The cooling rates produced by gas quenching were controlled by varying the gas flow and the relative quantities of He and Ar in the mixture flowing through the tubular chamber. These cooling rates could be directly quantified from the thermal history recorded by the pyrometer and were typically of the order of 10^2 K/s prior to nucleation and of the order of 10 K/s during solidification. Splat quenching is expected to produce cooling rates above $\sim 10^5$ K/s.[20] It should be noted, however, that the latter are not constant; high-speed video photography revealed that the anvils recoil after the initial impact and detach from the splat, although they rapidly close again and reestablish contact with the chill surfaces.

Most of the work in this area was done on alloy 5212 (1.15 pct B), but the effects are similar for all alloys above ~1 pct B, which could not be supercooled to any significant degree in the levitation experiments. The conventionally cast microstructure of 5212, shown in Figure 4(b), follows essentially the same solidification path discussed for alloy 5013 in Figure 6. The microstructural modifications arising from the enhanced cooling rate are illustrated in Figure 9. The most striking effect is on the shape of the borides, which are predominantly plates and needles at the slower cooling, ~5 K/s, but change almost completely to the convoluted flake morphology, with a relatively modest increase in quenching rate to ~15 K/s (compare Figures 9(a) and (b)). This is consistent with the general observation that the flakes are more abundant near the chill surfaces in arc buttons.

The higher solidification rates characteristic of splat cooling bring about much more significant changes in the microstructure. Figure 9(c) shows a partial cross-sectional view of a ~80 μm thick 5212 splat, with the chill zone on the left and the central region on the right of the micrograph. The small featureless zone on the chill side is associated with a nucleation event on the surface, from which the primary phase grows in a very fine microcellular pattern with segregate spacings smaller than ~0.5 μm (Figure 9(d)). As the cellular front moves away from the chill, the solidification rate decreases, partly

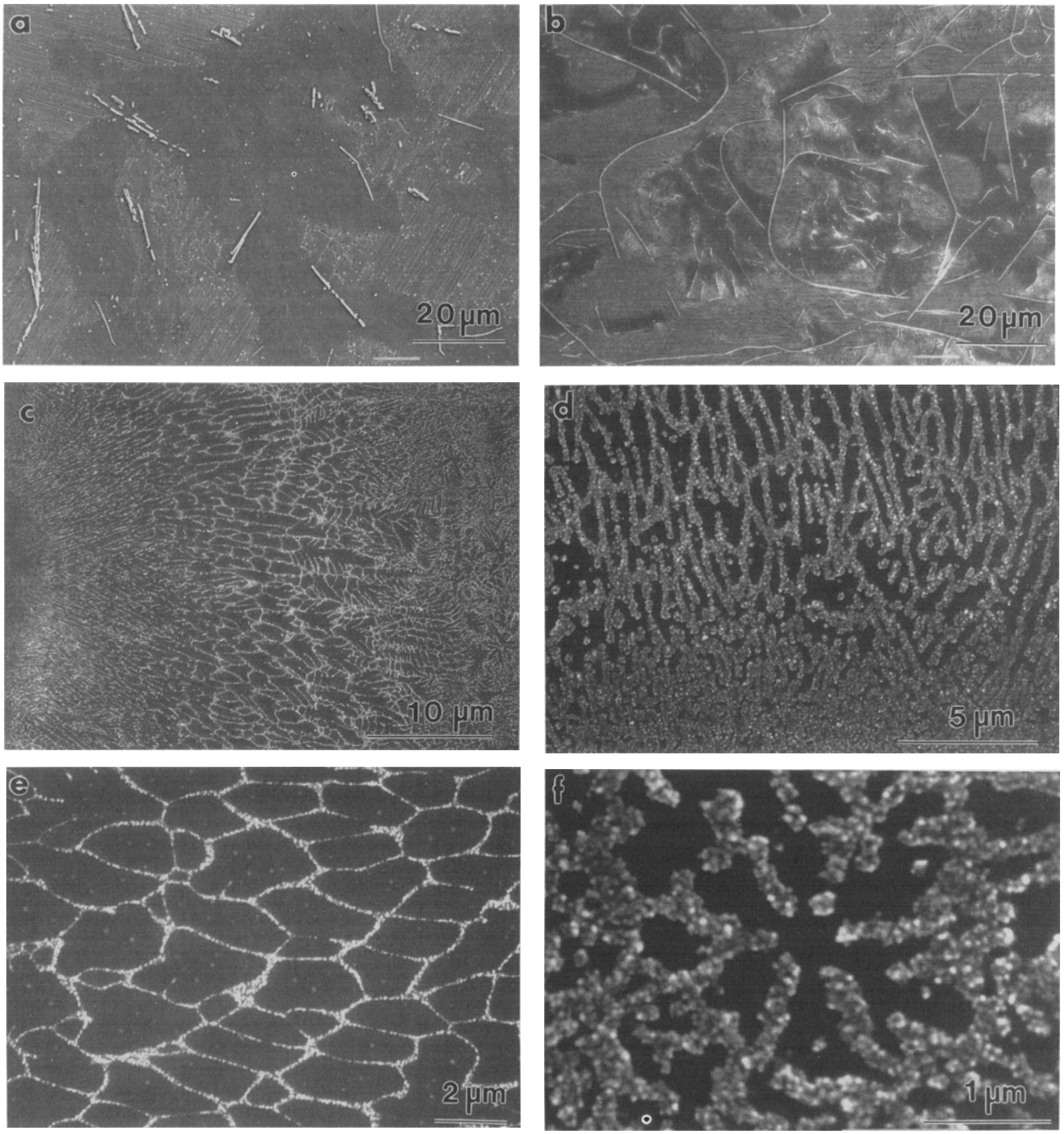

Fig. 9—SEM micrographs showing the effect of cooling rate on alloy 5212 (1.15 pct B). (*a*) Plates and needles observed after cooling at 5 K/s, but (*b*) only flakes present after cooling at 15 K/s; (*c*) cross-sectional view of one-half of a splat with the chill zone on the left side; (*d*) microcellular pattern near chill zone, (*e*) cellular/dendritic growth in the bulk of the splat, and (*f*) equiaxed α-Ti dendrite in the core of the splat. Boride regions are highly overetched in (d) and (f).

because of the inherent resistance to heat transfer imposed by the solid already formed and possibly because the splat detaches from the chill surface due to shrinkage and/or anvil recoil after the initial impact.* The cellular microstructure coarsens noticeably and starts to develop secondary branching, as seen in the middle section of Figure 9(c), with segregate spacings of 1 to 2 μm, as noted in Figure 9(e). Finally, the central region of the splat consists of equiaxed dendrites but with finer segregate spacings than those observed in the previous region (Figure 9(f)). This equiaxed zone could be ascribed to dendrite tip breakage due to the high flow velocities

*If bulk supercooling is achieved prior to nucleation, the ensuing recalescence would also be accompanied by a rapid drop in growth velocity.

which develop in the center plane of the droplet as it is squeezed into a splat. (This pattern of fluid flow out of the droplet center has been observed by high-speed video photography during the splat quenching experiments.) One might also speculate that the finer microstructural scale in the center is associated with an enhanced cooling rate, presumably due to the anvils re-establishing contact with the splat after the recoil event. However, the intractability of monitoring the thermal history in this process makes it difficult, if not impossible, to confirm this hypothesis.

The boride morphology and distribution also change dramatically in the splat-quenched material. The borides appear now as very fine equiaxed particles, similar to those observed in the highly supercooled samples ($\Delta T >$ 150 K), although in this case, they are clearly decorating the intercellular or interdendritic spaces (compare Figures 4(b) and 9(e)). The borides are also much finer in the splat, approaching in some cases the scale of the ultrafine platelets evolving from solid state precipitation (Figures 5(b) and 10(b)). Nevertheless, the concentration of particles in the interdendritic spaces indicates that the fine borides in the splat form as secondary phases during solidification rather than by precipitation from a supersaturated solid solution. The suppression of the flake morphology in favor of the fine equiaxed borides is indicative of an enhanced nucleation rate in the interdendritic melt, resulting from higher supersaturations concomitant to the increased solidification rate.

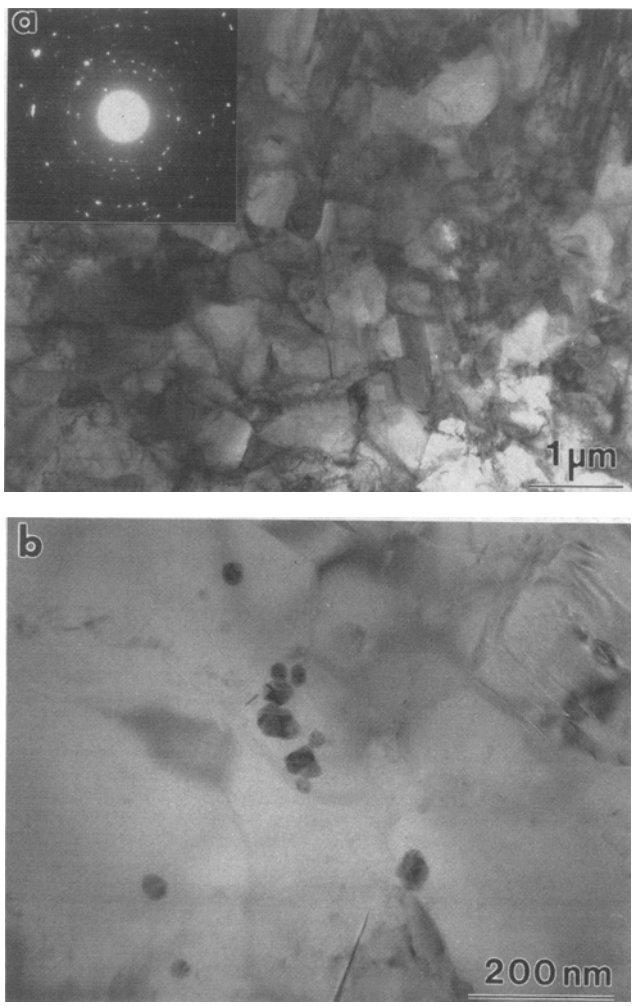

Fig. 10—TEM microstructure of a 5212 (1.15 pct B) alloy splat showing (*a*) fine polycrystalline γ matrix and (*b*) fine equiaxed boride particles within the γ grains.

It should be noted that the equiaxed dendrites—and even some of the columnar ones—often show a clearly hexagonal symmetry, as in Figure 9(f). This indicates that the primary phase in the splats is α-(Ti), and hence, that only moderate supercoolings were achieved in the liquid prior to nucleation. However, the TEM micrograph in Figure 10(a) shows the matrix in the center of the splat to be fine polycrystalline γ with grain sizes of the order of 500 nm and random orientations. In addition, the borides appear normally inside the γ grains, rather than at the grain boundaries (Figure 10(b)). These features can only be reconciled with the cast structure observed in the scanning electron microscope if the primary α phase transforms in the solid state to γ, possibly by growth from the γ present in the segregate regions at the end of solidification.

Epitaxial growth from the γ segregate has been previously observed in binary Ti-Al alloys during cooling but is normally superseded by the $\alpha \rightarrow \alpha_2$ ordering in the bulk of the dendrite. The latter gives way to the $(\alpha_2 + \gamma)$ lath structure by precipitation of γ plates at the stacking faults in the α_2 phase.[14,17] When the dendrite arms are relatively large ($\gg 1$ μm), the growth of γ from the segregate regions would only consume part of the dendrite before reaching the temperature where the ordering transformation becomes feasible. Note, however, that the segregate spacings in the splat are much smaller—of the order of the typical lath spacings in Figure 8(c)—suggesting that the density of sites for the growth of γ is sufficiently large to allow complete transformation of the primary α phase before the ordering temperature is reached. The absence of retained α_2, which is frequently found in binary Ti-Al alloy splats, reflects an enhanced driving force for the $\alpha \rightarrow \gamma$ transformation consistent with the relatively high Al:Ti ratio in the matrix ($\sim$1.1).

We have so far focused on the evolution of the matrix microstructure and the broader characteristics of the boride phases, *i.e.*, their shape and size, as well as their dependence on important solidification parameters like supercooling and cooling rate. It is clear at this point that some borides tend to exhibit plate and needle morphologies at the lowest solidification rates. Increasing the transformation rate, hence, the supersaturation, by either bulk supercooling or faster heat extraction gradually changes the morphology to convoluted flakes and, finally, to very fine equiaxed particles. We will now proceed to examine the borides in more detail and try to elucidate the differences in crystallography and growth mechanism of the different morphologies.

D. *Crystallographic Features of the Boride Phases*

Notwithstanding the variety of morphologies and sizes, all boride particles in the present study were positively identified as TiB_2 (C32) by TEM. The structure of TiB_2 consists of close-packed Ti planes (A) stacked with graphite-like boron planes (H) in an AH AH sequence along the *c*-axis of the crystal, as shown in Figure 11.[11]

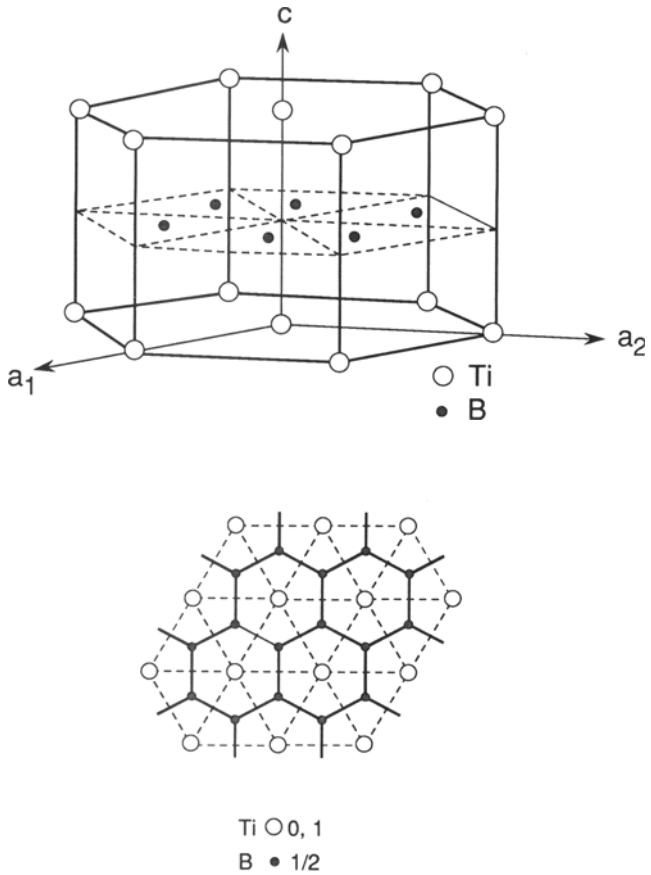

Fig. 11 — Crystal structure of TiB_2 showing the AH AH stacking of Ti and B layers along the *c*-axis. Note the difference in stoichiometry and stacking pattern of the $\{10\bar{1}0\}$ and $\{1\bar{2}10\}$ prismatic planes.

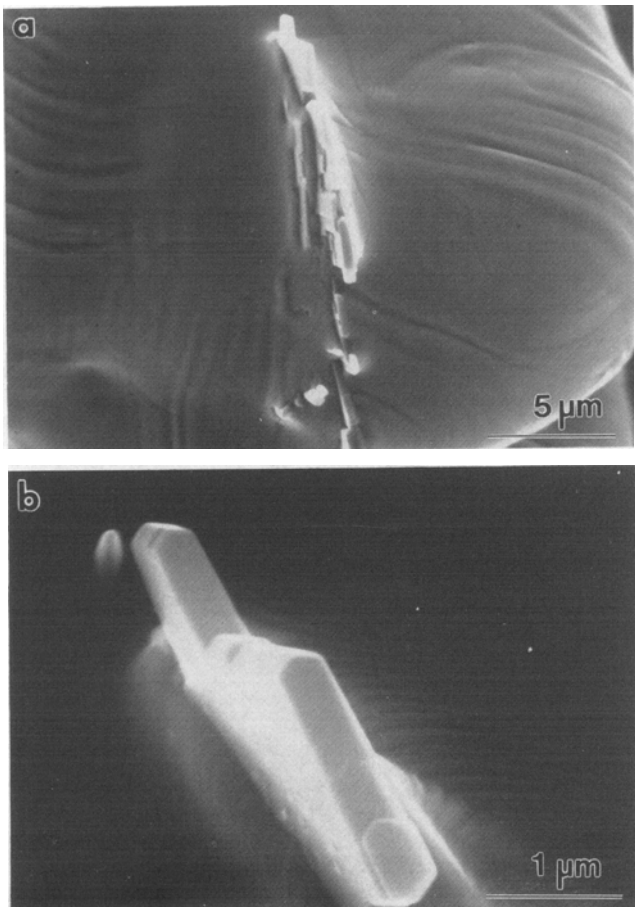

Fig. 12 — TiB_2 plates in the shrinkage cavity of a slowly cooled 5212 (1.15 pct B) alloy sample clearly showing (*a*) concurrent growth with the matrix and (*b*) basal and prismatic facets bounding the plate.

Growth of this phase is expected to take place by a ledge mechanism, whereupon the morphology would be determined by the slowest growing facets in the crystal. In the case where secondary borides grow from a melt dilute in boron, as in the present investigation, diffusional effects and physical constraints imposed by the matrix may also be relevant, as discussed below.

Crystals of primary TiB_2 growing from nearly equiatomic Ti-Al melts consistently show facets of the basal (0001) and prismatic $\{10\bar{1}0\}$ types.[11] Similar observations have been made on TiB_2 crystals growing unconstrained from various other melts,[21,22,23] suggesting that the growth rates normal to these planes are the slowest. This may be rationalized from the stacking sequence depicted in Figure 11, which in both cases involves alternate planes containing all-Ti and all-B atoms. Calculations of the attachment energy for various low-index facets of the TiB_2 crystal[23] suggest the following hierarchy of growth rates:

$$(0001) < \{10\bar{1}0\} < \{10\bar{1}1\} < \{1\bar{2}10\} < \{1\bar{2}11\}$$

The ranking essentially reflects the density of strong bonds (B-B > Ti-B > Ti-Ti) or "periodic bond chains"[24] in the various crystal planes.

Figure 12 shows TiB_2 plates found in the shrinkage cavity of a slowly cooled levitated sample of alloy 5212 (1.15 pct B). The borides are clearly embedded in a dendrite arm (Figure 12(a)), suggesting that they solidified concurrently with the matrix. The facets of the TiB_2 platelike crystals are still indicative of the hexagonal C32 geometry, as noted in Figure 12(b). Indeed, SAD analysis of an extracted plate-boride particle in Figure 13 shows the habit plane of the plate to be $\{10\bar{1}0\}$, whereupon the facets of the plate can be inferred to be of the basal and prismatic type. Thus, the growth mechanism is similar to that of the primary borides, but two of the prism directions are evidently constrained by the matrix, as shown in Figure 12(b), resulting in the elongated plate morphology.

Closer examination of the plates in deeply etched specimens revealed that they are often connected to needles in various stages of development (Figures 14(a) and (b)). The needles exhibit facets parallel to those of the plate, implying that they correspond to equivalent crystal planes but have a more equiaxed cross section. They seem to thicken by growth of prismatic ledges along the axis of the needle, as illustrated in Figure 14(c), and occasionally exhibit branching at angles which suggest a twin relationship between the original stem and the branch, as shown in Figure 14(d). Transmission electron microscopy analysis of an extracted needle in Figure 15 confirmed that the needle axis is indeed [0001] and the lateral facets are of the $\{10\bar{1}0\}$ type. Furthermore, small pyramidal facets of the $\{10\bar{1}1\}$ family were detected at the tip of the needle crystal in Figure 15(b), and extracted needles often showed angular tips suggestive of

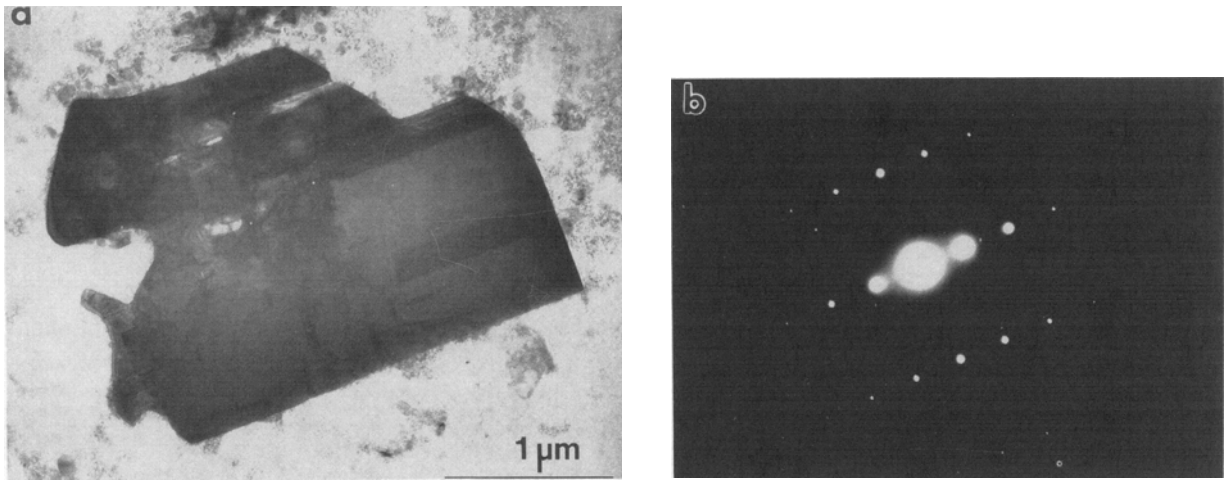

Fig. 13—TEM micrograph of a TiB_2 plate extracted from (*a*) a deep-etched specimen and (*b*) a diffraction pattern normal to the plane of the image showing a [10$\bar{1}$0] TiB_2 zone axis.

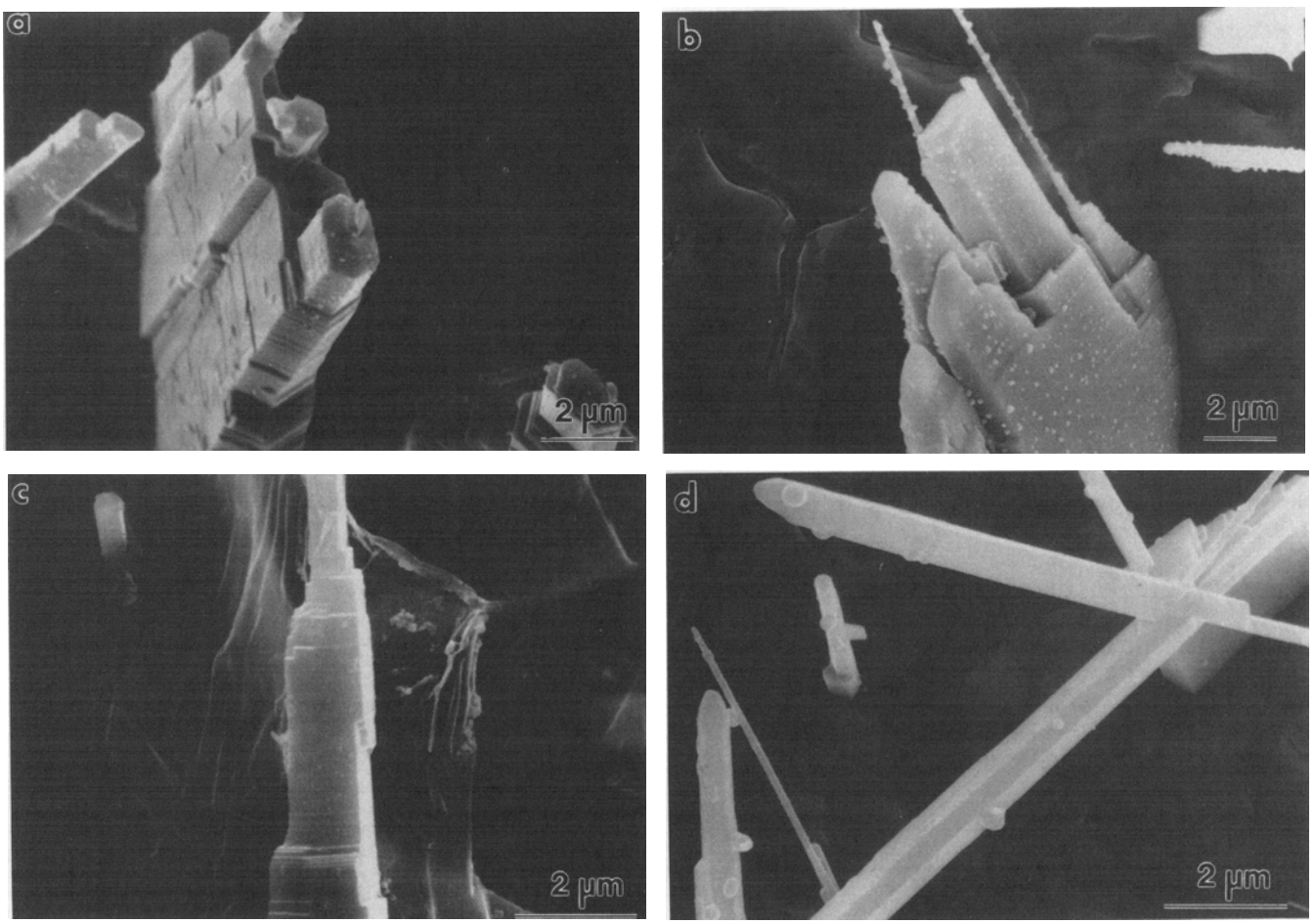

Fig. 14—Deeply etched arc button sections of alloy 5212 (1.15 pct B) showing (*a*) and (*b*) plates breaking into needles, (*c*) thickening of needles by prismatic ledges, and (*d*) branching of needles. Also note the angular tips of the needles, suggesting that they are bound by pyramidal planes.

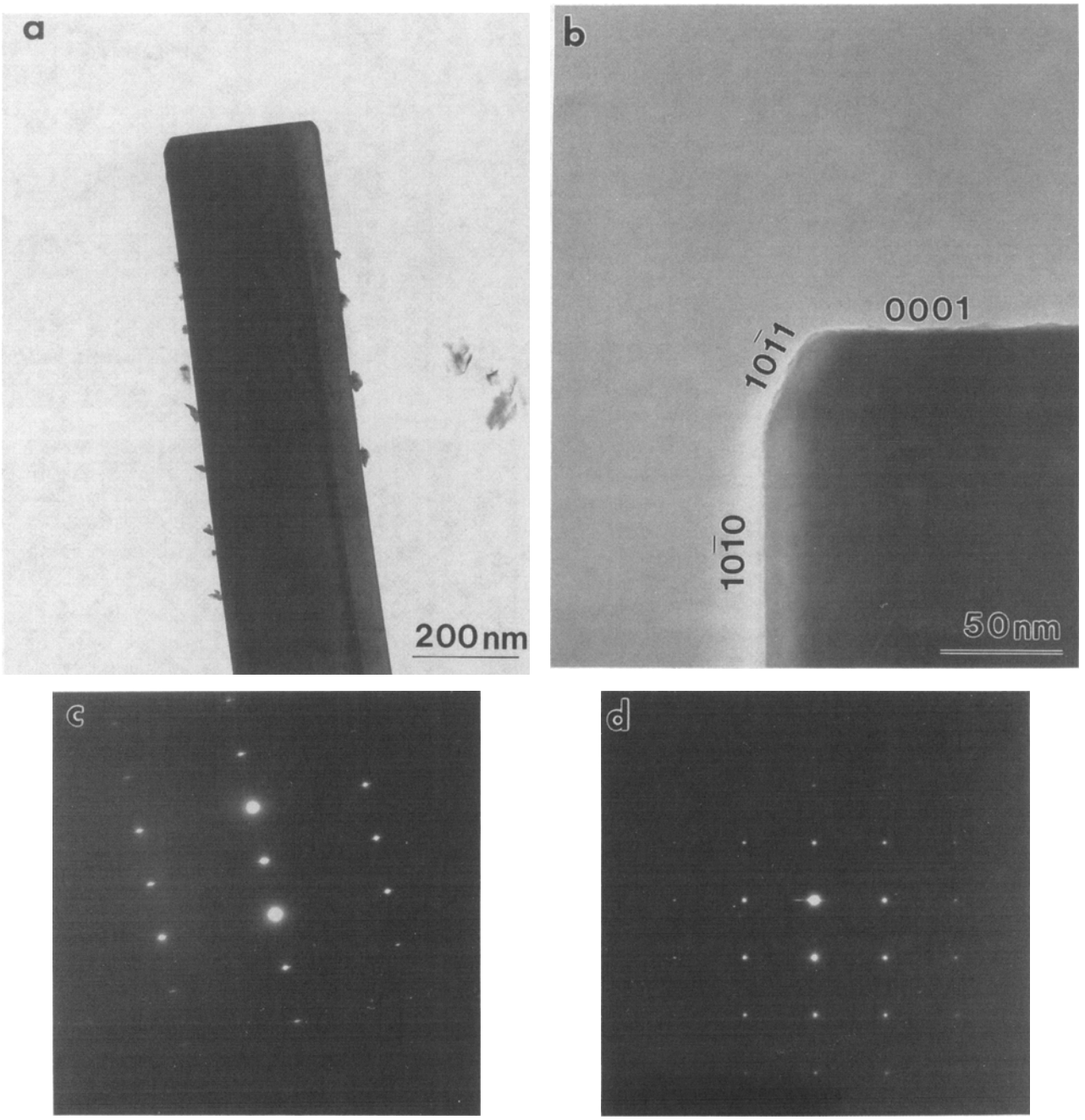

Fig. 15—TEM micrograph of an extracted TiB_2 needle showing the growth axis to be the [0001] direction of the TiB_2 crystal and a tip bounded by basal, prismatic, and pyramidal facets. The diffraction patterns in (c) and (d) correspond to the $[01\bar{1}0]$ and $[1\bar{2}10]$ zone axes of TiB_2, respectively.

growth bound by pyramidal planes (Figure 14(d)). These facets are probably responsible for the propagation of the needle tip along the *c*-axis, since growth normal to the basal plane is the slowest in TiB_2 and could not be easily reconciled with the development of the needle morphology.[23]

Figure 16 presents close views of the flake borides, which tend to be thinner and much longer than the plates and exhibit extensive meandering and branching, as previously seen in Figures 5, 7(c), and 9(b). Transmission electron microscopy analysis of flakes extracted from deeply etched samples (Figure 16(c)) confirmed that they are also TiB_2 but with a habit plane of the $\{1\bar{2}10\}$ type, as shown by the diffraction pattern in Figure 16(d). These higher index prismatic planes contain Ti and B atoms in the correct stoichiometric proportions and thus are expected to have lateral growth rates higher than those of the $\{10\bar{1}0\}$ prism facets (see ranking above). Ledge growth on the plane of the flake is clearly evident in Figures 16(b) and (c), where the ledges are parallel and perpendicular to the *c*-axis.

Finally, the small equiaxed borides produced at the higher supercoolings exhibit facets of the basal and $\{10\bar{1}0\}$ prismatic type like the plates and needles, as shown by

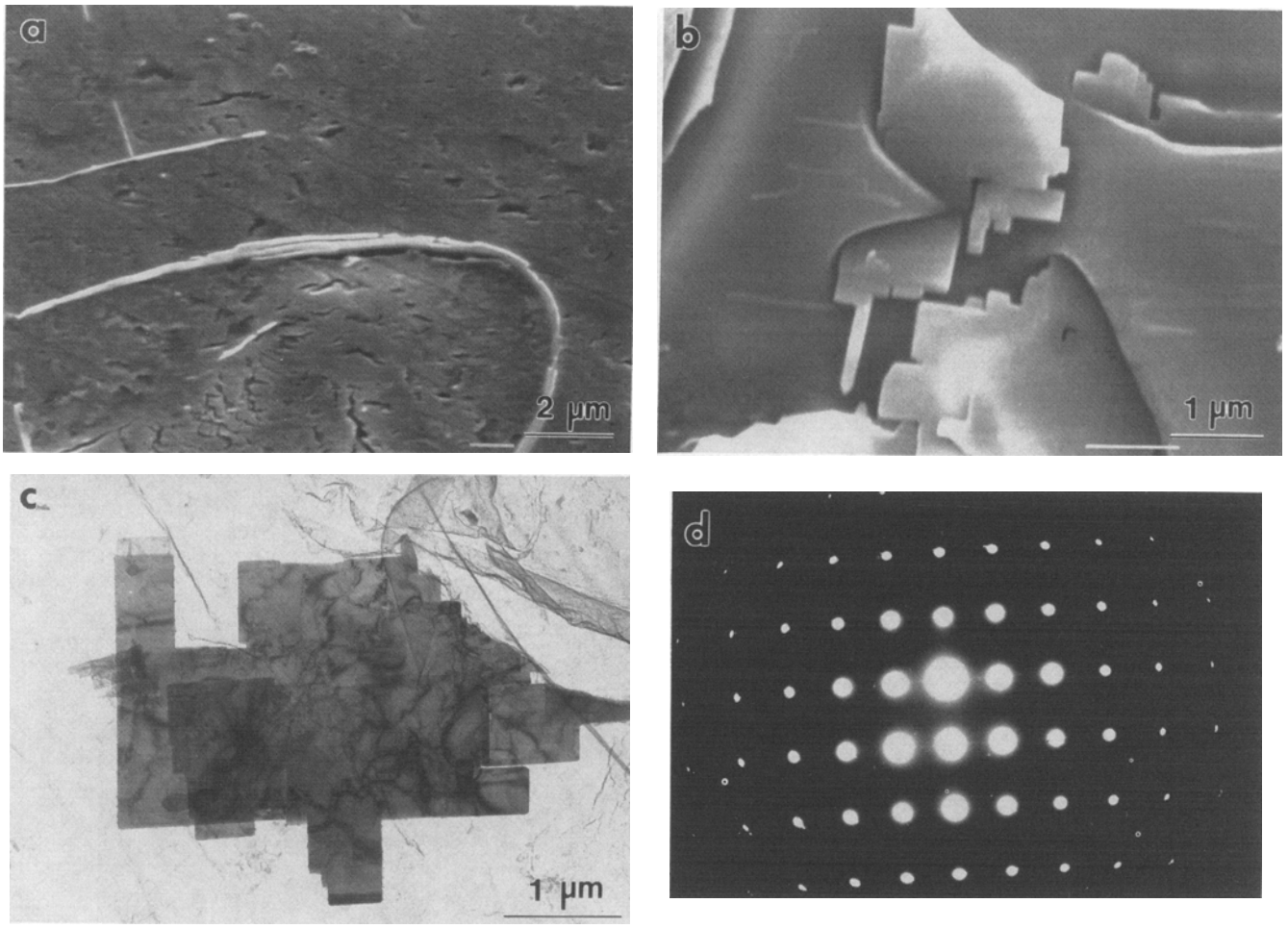

Fig. 16—SEM and TEM views of the TiB_2 flake morphology showing (*a*) a curved growth pattern with apparent layers within the flake, (*b*) thin flakes on the surface of a deep-etched specimen, (*c*) an extracted flake with the habit plane parallel to the plane of the image, and (*d*) the corresponding diffraction pattern with a $[1\bar{2}10]$ zone axis.

the TEM image and diffraction pattern in Figure 17. The facets of the finer interdendritic borides in the splat-quenched material are not as well defined as those in the supercooled samples (Figure 10(b)), although they are expected, in principle, to be of the same types.

E. *Evolution of the Boride Phases*

As noted before, it is clear at this point that the blocky particles nucleate and grow as primary phases from the melt for alloys with compositions within the TiB_2 region of the liquidus surface projection on Figure 6. All other particles in the conventionally solidified alloys (flakes/plates/needles) show evidence of having grown concurrently with the melt and may, in principle, be called "secondary" borides. The genesis of these multiple morphologies of secondary TiB_2 is rationalized below; the reader is referred to the comparative summary in Table II to aid in the following discussion.

The cast microstructures of the alloys leaner in B, *e.g.*, 5103 in Figure 5(a), show only flake borides clearly associated with the segregate, suggesting that the flakes are the "true" morphology for secondary TiB_2 in this system. This is consistent with the highly elongated and convoluted shape of the flakes, as well as their extensive branching, which would be expected for irregular (faceted/nonfaceted) eutecticlike solidification along the $L \rightarrow M + TiB_2$ monovariant line. Furthermore, the flakes have a habit plane and external facets different from the other "secondary" morphologies, presumably because of the need for faster propagation rates to sustain coupled growth with the matrix.

If the flakes are the "true" secondary boride morphology, one must then develop a rationale for the evolution of plates and needles. First, one may postulate from the observations on Figure 14 that the needles are not an independent morphology but, rather, a variant of the plates which arises from morphological instability of the boride-liquid interface owing to diffusional limitations to solute redistribution. Since TiB_2 contains 66 pct B and is growing from a melt with ~1 pct B, there is significant rejection of Ti and especially Al as the boride particles grow. Furthermore, Ti segregates preferentially to the metallic phase forming concurrently with TiB_2 (either α or γ), resulting in an effective enrichment of Al in the liquid phase (Figure 6). The needle

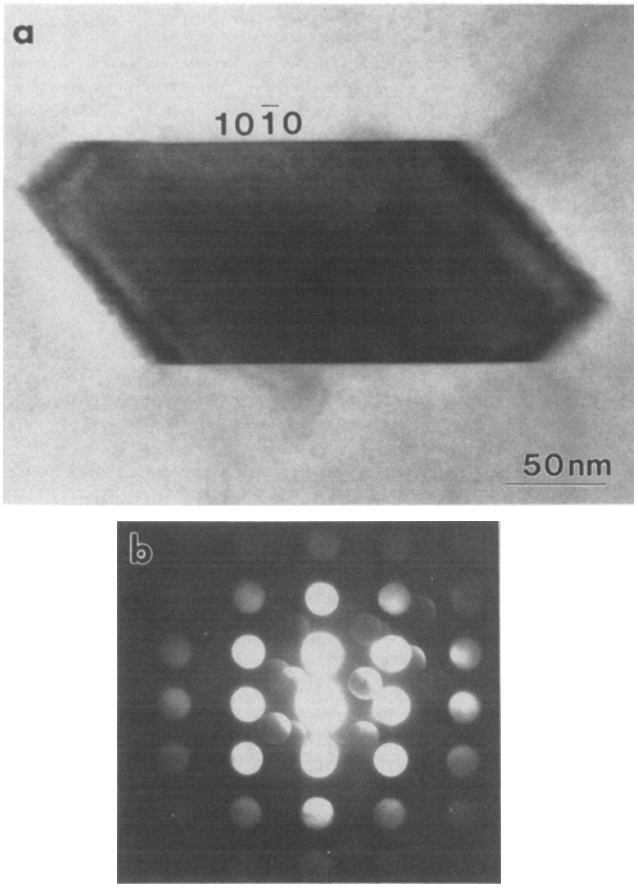

Fig. 17—(*a*) and (*b*) TEM image and diffraction pattern of the fine equiaxed TiB_2 found in the highly supercooled specimens. The facets shown are of the {10$\bar{1}$0} prismatic type. The zone axis of the diffraction pattern is [1$\bar{2}$16].

morphology is more efficient than the plate in optimizing the diffusional processes required for solute redistribution and should be favored as the liquid supersaturation increases. Thus, even though the growth mechanism involves essentially the same ledges in both plates and needles, the morphology changes in response to a diffusional constraint. Plate-to-rod transitions are quite common in faceted/nonfaceted systems with a low volume fraction of second phase, although their origin is still a subject of debate.[25]

We may now proceed to discuss the origin of the plates/needles as a single morphology different from the flakes. Since all three morphologies appear mixed with both dendrites (α) and segregate (γ), their origin cannot be ascribed to changes in the nature of the metallic phase growing concurrently with them. On the other hand, it is to be noted that the plates/needles exhibit facets which are identical to those of primary TiB_2, suggesting that they nucleate in the melt divorced from the matrix. The plates/needles are also consistently thicker than the flakes, even though the {1$\bar{2}$10} facets characteristic of the flakes should enable them to thicken faster than the plates/needles, which are bound by {10$\bar{1}$0} facets. Thus, one may infer that plates/needles are likely to have spent some time growing freely in the melt before they were trapped and constrained by the matrix, whereas the flakes nucleated and grew coupled with the matrix.

Based on the microstructural and crystallographic observations and on the sequence of evolution of the different morphologies with increasing B content, one may conclude that the plates/needles nucleate originally as primary TiB_2 slightly above the monovariant line. Since most of these alloys are dilute in B, the primary TiB_2 "seeds" do not grow or coarsen significantly before reaching the monovariant line, at which point the matrix phase nucleates. Once the latter appears, the existing TiB_2 "seeds" will be randomly trapped and evolve as plates/needles with the advancing liquid/solid interface, maintaining their original {10$\bar{1}$0} facets. On the other hand, truly secondary TiB_2 will also nucleate and grow as flakes coupled with the matrix along the $\alpha + TiB_2$ monovariant line.

As the supercooling (or cooling rate) increases in these alloys, formation of primary TiB_2 is progressively suppressed and fewer "seeds" will be present when the matrix phase appears, increasing the relative population of flakes. The latter are also favored because they can grow faster under higher supersaturations due to coupling with the matrix. One could readily establish an analogy between this behavior and that of a binary hypereutectic alloy that moves into the coupled zone as the solidification rate increases.[26,27] However, since this system involves a faceted/nonfaceted combination, the coupled zone would be skewed toward the phase with the highest kinetic hindrance,[28] *i.e.*, TiB_2. Thus, as the solidification rate increases, the interfacial temperature eventually falls below the coupled zone, where nucleation and growth of primary α (or β at higher supercoolings) is favored. Hence, the metallic phase evolves as cells or dendrites with TiB_2 forming as fine equiaxed particles divorced from the matrix in the supersaturated liquid behind the cellular/dendritic front.

IV. CONCLUSIONS

The solidification path for γ-TiAl alloys with 45–52 pct Al and dilute additions of B has been elucidated. The microstructural evidence suggests that the β, α, and γ liquidi emerging from the binary Ti-Al diagram meet the TiB_2 liquidus descending from the Ti-B binary along a monovariant line of the type $L \rightarrow M + TiB_2$. This line runs along the 1 pct B isoconcentrate in the Ti-Al-B ternary system, with the metallic phases M showing the same sequencing as in the binary, $M = \beta \rightarrow \alpha \rightarrow \gamma$. Therefore, except for the presence of the boride, solidification of the matrix in these alloys follows the same path as binary Ti-Al alloys of equivalent composition, forming primary β-(Ti) below ~49 pct Al and primary α-(Ti) dendrites above this composition. In principle, the interdendritic segregate is γ-TiAl in both cases, although its relative amount is only significant in the higher Al contents.

Alloys near the monovariant line exhibit three morphologies of the TiB_2 phase under conventional solidification conditions: flakes, plates, and needles. The flakes grow coupled with the matrix in the manner expected

for an irregular eutectic consisting of a faceted second phase in a nonfaceted matrix. The plates are believed to start as primary particles and should be present in alloys with B contents slightly above the monovariant line. These primary particles nucleate in the liquid and thus exhibit different crystallographic features from the flakes. However, they are subsequently trapped by the matrix which constrains their growth and induces them to develop anisotropic shapes. The needles are produced by breakdown of the plates due to morphological instability resulting from the diffusional boundary layer at the boride-melt interface.

Increasing the solidification rate produces transitions which are reminiscent of those of a hypereutectic alloy in a binary system with a faceted second phase. The initial effect is to suppress the formation of primary TiB_2 and to favor coupled growth, thus resulting in a predominance of the flake borides. Higher solidification rates promote the formation of primary α or β, with TiB_2 evolving as fine, divorced equiaxed particles in the interdendritic spaces. The selection of β at the higher supercoolings is consistent with the behavior of binary Ti-Al alloys of similar composition.

ACKNOWLEDGMENTS

This investigation was sponsored by the Defense Advanced Research Projects Agency under University Research Initiative Grant No. N00014-86-K-0753, supervised by Dr. William W. Barker and monitored by Dr. Steven G. Fishman of the Office of Naval Research. The authors are grateful to Dr. Ursula Kättner of the National Institute of Standards and Technology and Professor Y.A. Chang of the University of Wisconsin at Madison for discussions concerning the ternary diagram and to Dr. J.J. Valencia for his technical assistance in the early stages of this work.

REFERENCES

1. C.K. Elliott, G.R. Odette, G.E. Lucas, and J.W. Sheckherd: *High Temperature/High Performance Composites*, F.D. Lemkey, S.G. Fishman, A.G. Evans, and J.R. Strife, eds., MRS Symp. Proc., MRS, Pittsburgh, PA, 1988, vol. 120, pp. 95-101.
2. J. Rösler, T.C. Lu, and R. Mehrabian: University of California at Santa Barbara, unpublished research, 1990.
3. G. Bao, F. Genna, J.W. Hutchinson, and R.M. McMeeking: *Intermetallic Matrix Composites*, D.L. Anton, P.L. Martin, D.B. Miracle, and R.M. McMeeking, eds., MRS Symp. Proc., MRS, Pittsburgh, PA, 1990, vol. 194, pp. 3-14.
4. M.Y. He: *Intermetallic Matrix Composites*, D.L. Anton, P.L. Martin, D.B. Miracle, and R.M. McMeeking, eds., MRS Symp. Proc., MRS, Pittsburgh, PA, 1990, vol. 194, pp. 15-22.
5. L. Christodoulou, D.C. Nagle, and J.M. Brupbacher: U.S. Patent No. 4,751,048, June 14, 1988.
6. J.J. Valencia, C. McCullough, J. Rösler, C.G. Levi, and R. Mehrabian: in *Solidification of Metal Matrix Composites*, P. Rohatgi, ed., TMS, Warrendale, PA, 1990, pp. 133-50.
7. L. Christodoulou, P.A. Parrish, and C.R. Crowe: *High Temperature/High Performance Composites*, F.D. Lemkey, S.G. Fishman, A.G. Evans, and J.R. Strife, eds., MRS Symp. Proc., MRS, Pittsburgh, PA, 1988, vol. 120, pp. 29-34.
8. S.L. Kampe, J.A. Clarke, and L. Christodoulou: *Intermetallic Matrix Composites*, D.L. Anton, P.L. Martin, D.B. Miracle, and R.M. McMeeking, eds., MRS Symp. Proc., MRS, Pittsburgh, PA, 1990, vol. 194, pp. 225-32.
9. J.J. Valencia, J.P.A. Löfvander, J. Rösler, C.G. Levi, and R. Mehrabian: *Intermetallic Matrix Composites*, D.L. Anton, P.L. Martin, D.B. Miracle, and R.M. McMeeking, eds., MRS Symp. Proc., MRS, Pittsburgh, PA, 1990, vol. 194, pp. 89-96.
10. J. Rösler, J.J. Valencia, C.G. Levi, A.G. Evans, and R. Mehrabian: *Intermetallic Matrix Composites*, D.L. Anton, P.L. Martin, D.B. Miracle, and R.M. McMeeking, eds., MRS Symp. Proc., MRS, Pittsburgh, PA, 1990, vol. 194, pp. 241-48.
11. M.E. Hyman, C. McCullough, J.J. Valencia, C.G. Levi, and R. Mehrabian: *Metall. Trans. A*, 1989, vol. 20A, pp. 1847-59.
12. J.J. Valencia, C. McCullough, C.G. Levi, and R. Mehrabian: *Acta Metall.*, 1989, vol. 37, pp. 2517-30.
13. S. Krishnan, G.P. Hansen, R.H. Hauge, and J.L. Margrave: *Metall. Trans. A*, 1988, vol. 19A, pp. 1939-43.
14. C. McCullough, J.J. Valencia, C.G. Levi, and R. Mehrabian: *Acta Metall.*, 1989, vol. 37, pp. 1321-36.
15. C. McCullough, J.J. Valencia, C.G. Levi, and R. Mehrabian: *Mater. Sci. Eng.*, 1990, vol. A124, pp. 83-101.
16. Y.A. Chang, J.P. Neumann, and S.-L. Chen: *Alloy Phase Stability and Design*, G.M. Stocks, D.P. Pope, and A.F. Giamei, eds., MRS Symp. Proc., MRS, Pittsburgh, PA, 1990, vol. 186, in press.
17. M.J. Blackburn: in *The Science, Technology and Application of Titanium*, R.I. Jaffee and N.E. Promisel, eds., Pergamon Press, London, 1970, p. 633.
18. J.C. Williams: in *Precipitation Processes in Solids*, K.C. Russell and H.I. Aaronson, eds., TMS, Warrendale, PA, 1976, pp. 191-221.
19. S. Whang: *J. Mater. Sci.*, 1986, vol. 21, pp. 2224-38.
20. R.C. Rühl: *Mater. Sci. Eng.*, 1967, pp. 313-20.
21. I. Higashi and T. Atoda: *J. Cryst. Growth*, 1970, vol. 7, pp. 251-53.
22. K. Nakano, H. Hayashi, and T. Imura: *J. Cryst. Growth*, 1974, vol. 24–25, pp. 679-82.
23. A.A. Abdel-Hamid, S. Hamar-Thibault, and R. Hamar: *J. Cryst. Growth*, 1985, vol. 71, pp. 744-50.
24. P. Hartman: in *Crystal Growth: An Introduction*, P. Hartman, W. Bardsley, D.T.J. Hurle, and J.B. Mullin, eds., North-Holland Publishing Co., Amsterdam, The Netherlands, 1973, pp. 367-402.
25. R. Elliott: *Eutectic Solidification Processing*, Butterworth's, London, 1983, pp. 135-39.
26. W.J. Boettinger: in *Rapidly Solidified Amorphous and Crystalline Alloys*, B.H. Kear, B.C. Giessen, and M. Cohen, eds., North-Holland Publishing Co., Amsterdam, The Netherlands, 1982, p. 15.
27. R. Trivedi and W. Kurz: in *Solidification Processing of Eutectic Alloys*, D.M. Stefanescu, G.J. Abbaschian, and R.J. Bayuzick, eds., TMS, Warrendale, PA, 1988, pp. 3-34.
28. W. Kurz and D.J. Fisher: *Int. Met. Rev.*, 1979, vols. 5–6, pp. 177-204.